

STRUCTURE OF MERGER REMNANTS. V. KINEMATICS¹

JEREMY S. HEYL,² LARS HERNQUIST,³ AND DAVID N. SPERGEL⁴

Received 1995 March 6; accepted 1995 November 30

ABSTRACT

In this paper we report on a study of the kinematics of merger remnants. We have performed a series of numerical simulations of galaxy mergers, using a variety of orbital geometries and progenitor galaxies. Our analysis highlights three aspects of the kinematics of remnants: the misalignment of the total angular momentum of the luminous matter with respect to the minor axis of its spatial distribution; rotation curves along the major axis; and the distribution of luminous particles over the various allowed orbital families. By comparing the results from the various simulations, we learn how encounter geometry and the structure of the progenitors can affect the velocity distribution of the remnants. The encounter geometry, the structure of the progenitors, and the shape of the remnant play deciding roles in the distribution of angular momentum over the remnant, and therefore in the final velocity distribution.

We have employed a hybrid of two numerical techniques in our investigation. First, the encounter and the evolution of the remnant to equilibrium are simulated using a hierarchical tree algorithm. Once the remnant has settled down, we use a self-consistent field approach to study its orbit structure, thereby mitigating the scattering of particles between orbit families owing to two-body interactions. With this hybrid, a reliable determination of the orbital distribution of particles is practical.

Subject headings: galaxies: interactions — galaxies: kinematics and dynamics — galaxies: structure — methods: numerical

1. INTRODUCTION

When astronomers began to observe the velocity distributions of elliptical galaxies a number of peculiarities were discovered. Bertola & Capaccioli (1975) and Illingworth (1977) found that large elliptical galaxies rotate too slowly to account for their shapes. No longer could ellipticals be interpreted as simple oblate rotators, but rather anisotropic velocity distributions were evoked to explain their triaxial structure. Even more intriguing features were uncovered when elliptical galaxies were observed in greater detail. Franx, Illingworth, & Heckman (1989) found that the apparent rotation axis of an elliptical galaxy need not coincide with its apparent minor axis, supporting the view that ellipticals are triaxial. For an axisymmetric oblate rotator, the axis of rotation will always lie along the apparent minor axis, but in triaxial distributions supported by velocity anisotropy, the rotation axis and the minor axis need not be aligned.

The merger hypothesis for the origin of elliptical galaxies (Toomre & Toomre 1972; Toomre 1977) argues that elliptical galaxies form through the merger of spiral galaxies and other “late-type” systems. In light of this proposition many questions arise. In general, what are the dynamical signatures of merger remnants? Can stellar dynamical mergers reproduce the kinematic features of elliptical galaxies? What is the physical basis for these features?

We explore the consequences of the merger hypothesis for the expected velocity distributions of elliptical galaxies by analyzing N -body simulations of galaxy mergers. The simulations employ a variety of initial orbits (prograde, retrograde, and skew encounters) and progenitor models

(disks without bulges and disks with rotating bulges). These calculations extend those of Barnes (1992), and we concur with his main conclusions.

In the following sections, we describe the simulations (§ 2), the velocity profiles of merger remnants (§ 3), including the measurement of misalignment angles and their errors (§ 3.3), and an analysis of the orbits of merger remnants (§ 3.4). We conclude with a discussion of implications of our results (§ 4).

2. THE SIMULATIONS AND ANALYSIS

The simulations examined here are part of an ongoing series studying the nature of remnants produced by the mergers of galaxies resembling the Milky Way (Hernquist 1992; Hernquist & Spergel 1992; Spergel & Hernquist 1992; Hernquist 1993a; Hernquist, Spergel, & Heyl 1993; Hernquist, Heyl, & Spergel 1993; Heyl, Hernquist, & Spergel 1994; Heyl, Hernquist, & Spergel 1995). The self-gravity of the system is calculated with a hierarchical tree algorithm (Barnes & Hut 1986), which has been further optimized for use with vectorizing supercomputers (Hernquist 1987; Hernquist 1990a; Hernquist & Katz 1989). Rather than scaling as $\sim O(N^2)$ as direct summation, the “tree” method scales as $\sim N \log N$, making possible simulations with upwards of a quarter of a million particles.

2.1. Review of the Simulations

For our purposes here, a quick review of the system of units and the initial conditions is appropriate. We first take G equal to 1, and by scaling the mass to the Galaxy, we derive the following natural set of units for time, mass, and length, respectively, 1.31×10^7 yr, $5.6 \times 10^{10} M_\odot$, and 3.5 kpc. Unit velocity then corresponds to 263.3 km s^{-1} . From simulation to simulation we varied the initial geometry of the encounter and the structure of the progenitor galaxies. We refer to each simulation by means of its run code. These codes are summarized in Table 1. A detailed discussion of the initial conditions may be found in Paper IV (Heyl et al. 1994) and in Hernquist (1993b).

¹ Lick Observatory Bulletin No. B1329.

² Institute of Astronomy, Madingley Road, Cambridge CB3 0HA, UK; Department of Physics, South Road, University of Durham, Durham DH1 3LE, UK; present address: Lick Observatory, University of California, Santa Cruz, Santa Cruz, CA 95064.

³ Sloan Foundation Fellow, Presidential Faculty Fellow; Lick Observatory, University of California, Santa Cruz, Santa Cruz, CA 95064.

⁴ Princeton University Observatory, Princeton, NJ 08540.

TABLE 1
RUN CODES

Run Code	Description
NB00.....	Neither progenitor has a bulge, and both disks rotate prograde with respect to the orbit
RB00.....	Both progenitors have rotating bulges and both disks rotate prograde with respect to the orbit
NB02.....	Neither progenitor has a bulge, and one disk rotates retrograde
NB01.....	Neither progenitor has a bulge, and one disk is tilted with respect to the orbit plane
NB11.....	Neither progenitor has a bulge, and both disks are tilted with respect to the orbit plane
RB11.....	Neither progenitors have rotating bulges, and both disks are tilted with respect to the orbit plane
NB22.....	Neither progenitor has a bulge, and both disks rotate retrograde

To model an encounter and merger, each progenitor galaxy is resolved with 131,072 particles evenly split between a disk and halo component. Some progenitors have bulge components. Each bulge contains an additional 16,384 particles. The total number of particles in a simulation is either 262,144 or 294,912, depending on the presence of the bulge. Each simulation is evolved for 144 time units or 1.9×10^9 yr. First, pericenter is reached about 24 time units after a calculation begins. For all but one simulation we consider the potential of the remnant to have reached a steady state by the end of the computation. For the remaining simulation (NB00) we followed its evolution for an additional 48 time units. This remnant suffers a firehose instability which does not phase-mix until $t = 192$. A discussion focusing on this simulation appears in Hernquist, Heyl, & Spiegel (1993).

2.2. Orbit Classification

To classify individual orbits, we follow the method devised by Barnes (1992). For each orbit, we count the number of times the sign of each component of the angular momentum changes during the analysis; we take the x -axis to be the major axis, the y -axis to be the intermediate axis, and the z -axis to be the minor axis. Since the entire system is rotated to conform with the principle axes of the remnant, the classification is simple. If the signs of all three components of a particle's angular momentum change, it is traveling on a box orbit. If only the sign of the component along the x -axis does not change, it is on a major-axis tube orbit. Finally, if only the sign of the z component is unchanging, we have a minor-axis tube. Of course, some degeneracy remains. A small fraction of the orbits will have neither the x component nor y component change. We are thus left with eight classes as shown in Table 2. Furthermore each of these classes (except for the box orbits) may be divided into two subclasses depending on whether the circulation about the axis is clockwise or counterclockwise.

When information supplied by the sign changes is combined with the finding that the intermediate axis does not parent an orbit family (Binney & Tremaine 1987) and that the major-axis and box orbits tend to have shorter orbital timescales, we get the "likely" classifications listed in Table 2. To reduce the number of ambiguous classifications, the orbits are classified for only the 75% most tightly bound

TABLE 2
ORBIT CLASSES

DESCRIPTION	CHANGE IN SIGN		
	L_x	L_y	L_z
Box	Yes	Yes	Yes
Major-axis tube	No	Yes	Yes
Likely box	Yes	No	Yes
Likely major-axis tube	No	No	Yes
Minor-axis tube	Yes	Yes	No
Likely minor-axis tube	No	Yes	No
Likely minor-axis tube	Yes	No	No
Likely minor-axis tube	No	No	No

luminous particles. On average, $\sim 10\%$ of the orbits fall into the "likely" categories.

2.3. Self-Consistent Field Method

To calculate orbits, the potential is expanded in spherical harmonics and a radial set of eigenfunctions based on the Hernquist density profile (Hernquist 1990b) by means of a self-consistent field (SCF) method (Hernquist & Ostriker 1992). The self-consistent field method is less sensitive to direct interactions between pairs of particles which may scatter particles from one orbit family to another during the analysis than direct N -body methods.

The SCF analysis begins with the final snapshot of the TREECODE simulation. We calculate the expansion coefficients of the potential to sixth order ($n_{\max} = 6$) in the radial direction and to fourth order ($l_{\max} = 4$) in spherical harmonics using the final positions of all the particles (dark and luminous). Once the coefficients in the expansion have been calculated, the potential is frozen for the remainder of the analysis.

Next we select the particles to be analyzed. First, to find the center of the remnant, we calculate the center of mass for only the luminous particles located where the potential was less than -2 . This includes $\sim 60\%$ – 70% of the luminous particles. We then calculate the moment of inertia of these same particles and rotate the entire remnant such that the major axis is aligned along the x -axis, the intermediate along the y -axis, and the minor axis is aligned along the z -axis. Neither the determination of center of mass nor of the principle axes is strongly affected by changes in the potential cutoff. This rotation simplifies the bookkeeping of the orbit analysis. Finally, we reduce the number of particles by a factor of 16 from approximately 260,000 particles to 17,000 particles for subsequent integrations.

The orbital period of a particle at the half-mass radius for the luminous material is approximately six time units; therefore, we choose to follow the orbits of the 17,000 remaining particles for 24 time units, counting the number of times each component of the angular momentum changes along each orbit. This choice allows the orbit analysis to converge with few orbits being placed in one of the "likely" categories while minimizing the effects of figure rotation.

To ensure that we are not undersampling the potential, we repeat the orbit analysis for two of the runs with $n_{\max} = 8$ and $l_{\max} = 6$. Also, to verify that our expediency of freezing the potential does not grossly affect the classification of orbits, we perform the same analysis with the full number of particles and recalculate the expansion coefficients and principal axes at every time step. As evident from Table 3,

TABLE 3
EFFECT OF SIMPLIFICATION ON ORBIT ANALYSIS

Run Code	n_{\max}	l_{\max}	Particle Number	f_{box}	$f_{\text{major tube}}$	$f_{\text{minor tube}}$
NB00.....	6	4	16,384	0.620	0.132	0.248
	8	6	16,384	0.621	0.136	0.244
	6	4	262,144	0.670	0.065	0.264
NB02.....	6	4	16,384	0.617	0.027	0.356
	8	6	16,384	0.623	0.021	0.356
	6	4	262,144	0.601	0.020	0.379

these simplifications only affect the orbit analysis at a level of a few percent of the total number of orbits with the strongest effect being on the number of major-axis tube orbits.

The two simulations chosen also provide an opportunity to assess the effects of figure rotation. The remnant in run NB00 rotates $\sim 1^\circ$ per time unit or $\sim 25^\circ$ during the duration of the analysis. Our classification method does not take into account figure rotation, but when we freeze the potential for the 17,000 particle simulations, we effectively freeze the figure as well. So in the rotating analysis, the principal axes rotate along with the orbit families. Consequently, some (approximately one-third) of the former major-axis tubes are reclassified as boxes, and an additional one-sixth are classed as minor-axis tube orbits. While in run NB02 whose remnant rotates much more slowly, this effect is absent. As run NB00 has the most quickly rotating figure, it provides an upper bound on the error that we introduce when we ignore figure rotation.

3. VELOCITY DISTRIBUTIONS

3.1. Light-of-Sight Velocity Distributions

The light-of-sight velocity distribution (LOSVD, following Rix & White 1992) is usually characterized by only its first two moments: the mean (the bulk velocity of the galaxy) and the velocity dispersion. Unless one has high-quality spectra, this is the most one can expect to get. But recently observers have developed techniques to extract a more detailed picture of LOSVDs from spectra of elliptical galaxies (Rix & White 1992; Bender 1990; Franx & Illingworth 1988; van der Marel et al. 1994). Here we calculate LOSVDs for the remnants as a whole from a variety of orientations for the entire remnant. From the simulation, the calculation of the various moments is straightforward: once the line-of-sight vector is determined, one needs only to sum the dot product of the velocity vector with the line of sight over the luminous particles in the simulation. For a better comparison with observations, we calculate the moments only for the particles within one half of the half-light radius ($0.5r_e$) in projection.

First, we select a viewpoint from 254 viewpoints uniformly distributed over a sphere. Next we calculate the projected positions and radial velocities of all the luminous particles in the simulation, and sort them by radius from the projected center of light to find the projected half-light radius (r_e). Finally, the moments are calculated by summing over all the particles within $r_e/2$. Effectively, we place an aperture of radius $r_e/2$ over the remnant, measure a spectrum, and calculate the moments from this spectrum. We repeat this process for the remaining 253 viewpoints for each remnant to find orientation-independent (and orientation-dependent) properties of these moments.

To concisely describe the LOSVDs of the remnants we use the velocity dispersion, skewness (\mathcal{S}), and the kurtosis (\mathcal{K}). These traditional statistics are comparable to the Gauss-Hermite (G-H) moments (van der Marel & Franx 1993; van der Marel et al. 1994; Gerhard 1993; Heyl, Hernquist, & Spergel 1995). The latter are defined by (Press et al. 1986)

$$\mathcal{S} = \frac{1}{N} \sum_{j=1}^N \left(\frac{v_j - \bar{v}}{\sigma} \right)^3 \pm \sqrt{\frac{15}{N}}, \quad (1)$$

$$\mathcal{K} = \left[\frac{1}{N} \sum_{j=1}^N \left(\frac{v_j - \bar{v}}{\sigma} \right)^4 \right] - 3 \pm \sqrt{\frac{96}{N}}.$$

The error values apply exactly only if the underlying distribution is a Gaussian. Therefore, here they merely provide estimates. In our case $N = 131,072$, which yields errors of order 0.01 and 0.03, respectively.

To test our algorithm, we generate a 130,000 particle Plummer model with unit mass and scale length, and calculate the various moments within several apertures from 254 viewpoints evenly distributed on a sphere. The model is truncated at a radius of 20 units. Our merger simulations also have approximately 130,000 luminous particles, so this also provides an estimate of the errors in the various moments. Table 4 presents the results for the dispersion, skewness, and kurtosis. Both the random errors of the algorithm and the systematic deviation are quite small.

Here, we focus on the skewness. The even moments correlate well with each other and the orientation of the remnant (Heyl et al. 1995). On the other hand, this odd moment distinguishes amongst the remnants. Because the mean skewness (or the mean of any odd G-H moment) is zero for a uniform set of viewpoints by symmetry, to understand skewness we focus on its magnitude, not its sign. Therefore, we calculate the dispersion in the value of the skewness for the merger remnants, as shown in Table 5. Two strong trends are evident. First, the skewness tends to be larger in magnitude for the remnants of mergers of bulgeless galaxies than in the bulge-disk simulations. Second, the skewness is larger for simulations with “messier” initial

TABLE 4
RESULTS FOR PLUMMER MODEL

RADIUS	THEORY			SIMULATION		
	σ_R	\mathcal{S}_R	\mathcal{K}_R	σ_R	\mathcal{S}_R	\mathcal{K}_R
0.5.....	0.3737	0	-0.363	0.3737 ± 0.0010	0.000 ± 0.011	-0.357 ± 0.018
1.0.....	0.3563	0	-0.340	0.3566 ± 0.0004	0.001 ± 0.008	-0.341 ± 0.011
10.....	0.3147	0	-0.059	0.3157 ± 0.0003	0.000 ± 0.006	-0.075 ± 0.011
20.....	0.3137	0	-0.042	0.3141 ± 0.0003	0.000 ± 0.005	-0.050 ± 0.007

TABLE 5
DEVIATION IN SKEWNESS

Run Code	$\sigma_g \times 10^3$
NB00.....	18.3
RB00.....	8.8
NB02.....	34.6
NB01.....	36.2
NB11.....	46.2
RB11.....	20.2
NB22.....	44.1

conditions; that is, simulations which began with at least one of the disks skew to the initial orbit or rotating retrograde with the orbit. Evidently the first trend is stronger; the skewness of RB11, a really “messy” collision is only slightly larger than NB00, a “clean” collision. Figure 1 shows the distribution of the absolute value of the skewness for the eight simulations, divided into groups based on whether or not the progenitors had bulges and how “messy” the initial conditions were. In the following sections, we will show that kinematics can betray the origins of the remnants in a number of ways.

3.2. Major-Axis Profiles

Without the possibility of the transfer of angular momentum, mergers could never occur. Qualitatively, during a merger, the angular momentum contained in the relative orbit of the inner, more dense components is transferred outward to the less dense components and is transformed into rotation. The main mechanism for this transfer is dynamical friction which slows the motion of the denser components relative to the less dense background. Thus, in the final remnant, one would expect the amount of deposited angular momentum to increase with decreasing density and therefore to increase with radius.

How is this transfer of angular momentum manifest in the merger remnants? Figures 2 and 3 show the major-axis velocity profiles of the remnant NB00 as viewed from two points in the initial orbital plane. From both viewpoints, we observe a nearly linear increase in the streaming velocity of particles in the remnant. This linear increase is a signature of the angular momentum transfer and is apparent in all the remnants from many orientations.

The two viewpoints yield mainly differences in the magnitudes of the various quantities. From the viewpoint along the major axis of the remnant (Fig. 2), we see a velocity dispersion of approximately 190 km s^{-1} and a peak streaming velocity of 60 km s^{-1} . The accompanying plot shows the profiles from a viewpoint near the intermediate axis (the minor axis of the remnant is vertical in the figures). It has a dispersion of only 160 km s^{-1} and a smaller peak streaming velocity of 30 km s^{-1} . As discussed in the previous section, we again see that the velocity profiles of the remnant strongly depend on viewpoint. When one considers the shape of the remnant in run NB00 along with the change in viewpoint, the differences in the profiles do not appear so surprising. As the remnant is supported by a combination of velocity anisotropy and rotation, one would expect to observe both higher velocity dispersions and streaming motions when one looks along the major axis of the remnant. Figures 4 and 5 depict the profiles for the nearly spherical remnant of run RB11 viewed from two viewpoints. The projected shape of the remnant changes little as we change viewpoints, but the change in the profiles is striking.

Recently, Hui et al. (1995) observed planetary nebulae in the galaxy NGC 5128 to determine the dynamics of this suspected merger remnant beyond 4 times the effective radius. They find that the rotation velocity of the planetary nebula population increases markedly from the center to the outskirts of the galaxy. This increase is accompanied by a decrease in the velocity dispersion. The velocity field of

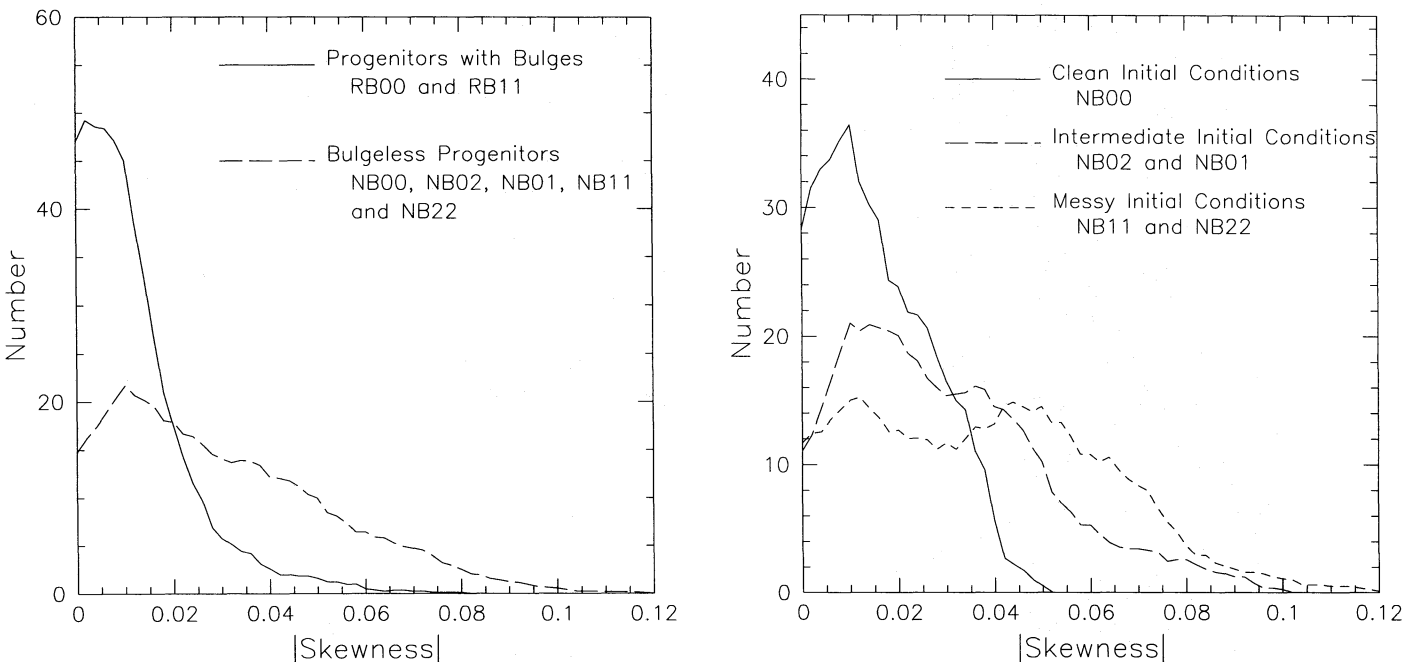


FIG. 1.—Skewness correlates with the properties and initial conditions of the progenitors. The left panel depicts the distribution of the absolute value of the skewness over several orientations for the remnants resulting from progenitors with bulges versus those without. The right panel compares the remnants resulting from collisions without bulges for several initial orbits. The distributions are normalized to have equal areas.

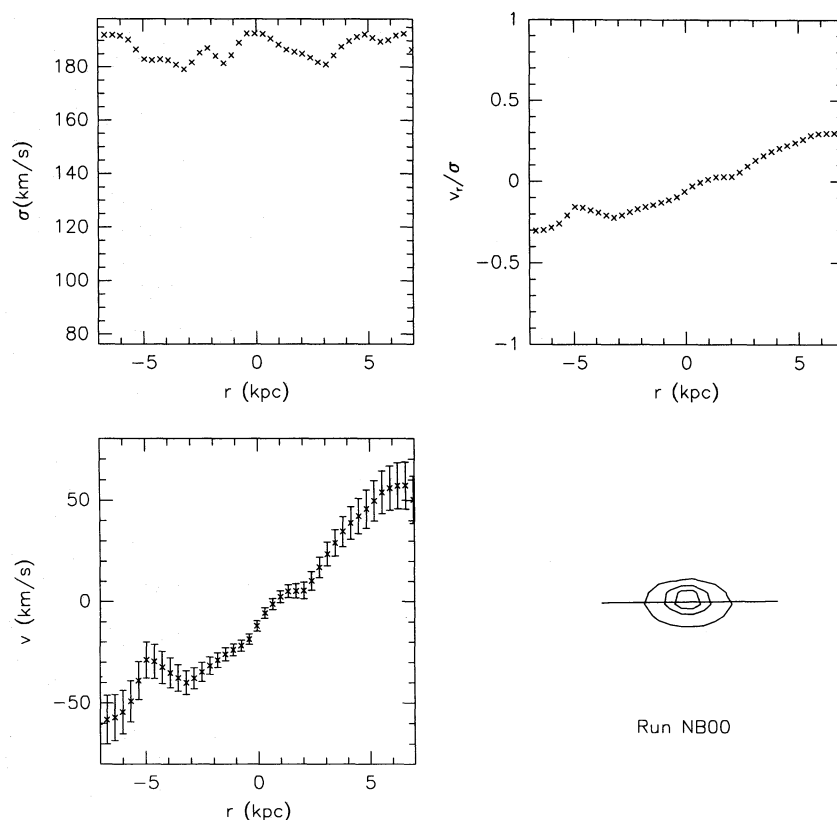


FIG. 2.—Major-axis velocity profile of the remnant NB00 from a viewpoint in the plane of the initial orbit. The view looks down the long axis of this nearly prolate remnant. The shape of the remnant and the “slit” along which we measured the profile are depicted in the lower right panel.

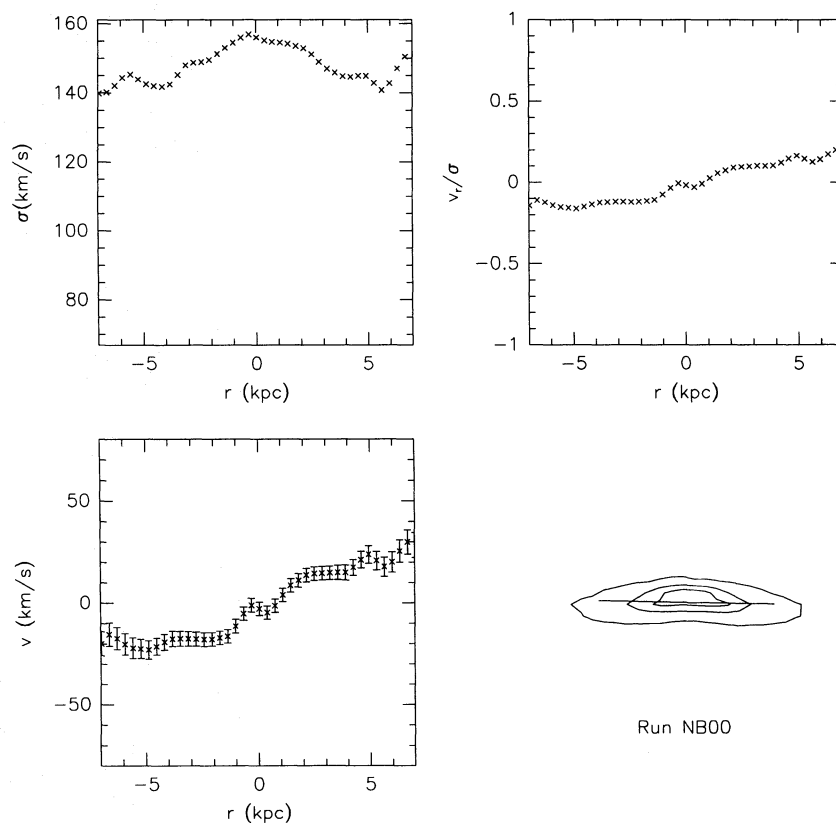


FIG. 3.—Major-axis profile of the remnant NB00. This figure is analogous to the preceding figure except that the remnant has been rotated through 90° . This viewpoint is also in the plane of the initial orbit.

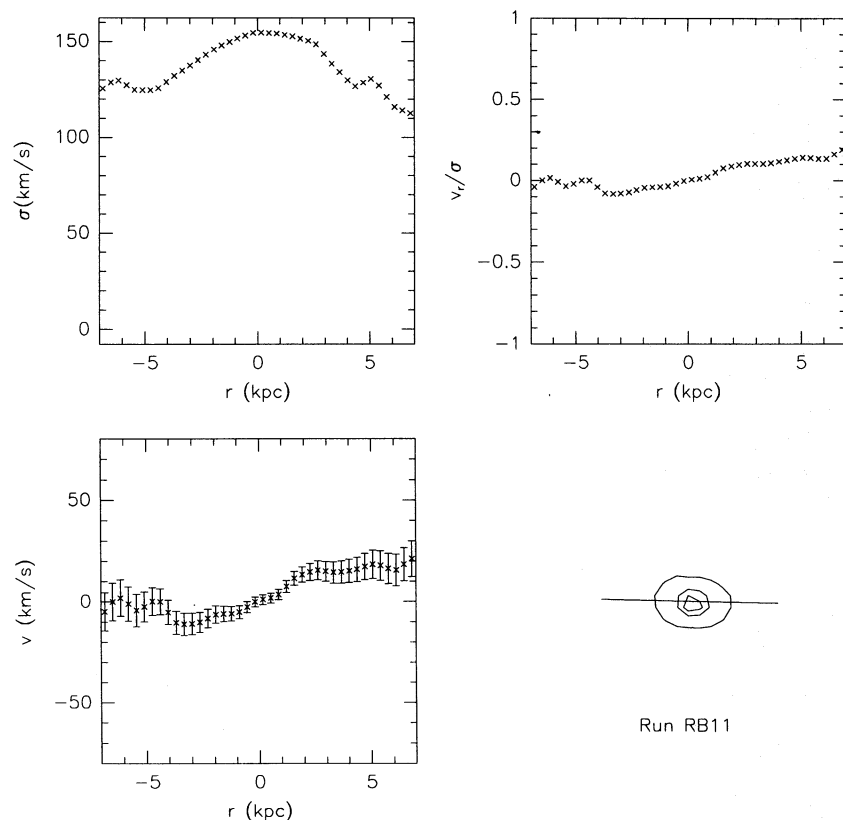


FIG. 4.—Major-axis velocity profile of the nearly spherical remnant RB11 from a viewpoint in the plane of the initial orbit

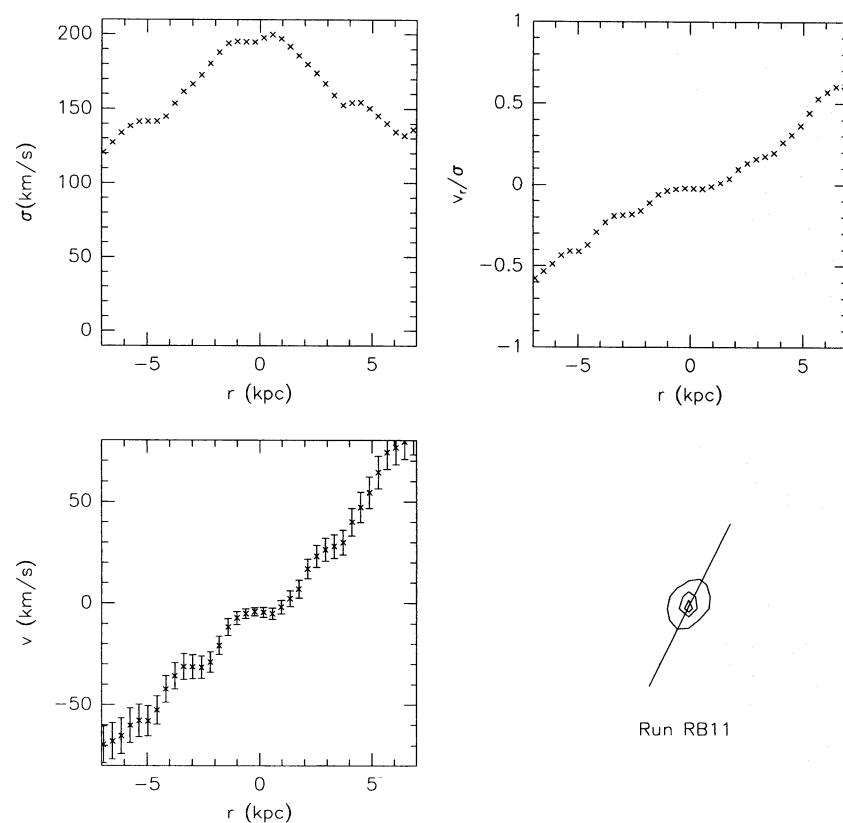


FIG. 5.—Major-axis velocity profile of remnant RB11. This figure is analogous to the preceding figure except that the remnant has been rotated through 90° . This viewpoint is also in the plane of the initial orbit. A comparison with the preceding figure shows the strong dependence of the velocity profile on the viewpoint, especially for remnants resulting from skew encounters.

this galaxy is remarkably similar to that of remnant RB11 as shown in Figure 5. Both in the remnant and NGC 5128, the rotation velocity increases from zero at the center to 80 and 90 km s⁻¹ (for the simulation and the galaxy respectively) at $2r_e$. This increase is accompanied by a decrease in the dispersion from 200 to 120 km s⁻¹ in the RB11 and 150 to 100 km s⁻¹ in the galaxy.

The kinematic features that we find in the merger remnants are also evident in ordinary usual elliptical galaxies. Some of Franx et al. (1989) sample of 22 elliptical galaxies exhibit features seen in the merger remnants. Two galaxies (NGC 1395 and NGC 1407) show a linear increase in streaming velocity similar to that seen in the remnants, and another five show this feature more weakly. Furthermore, nearly half of their galaxies show a marked decrease of σ with radius as seen in remnant RB11. For comparison, in Figure 6 we plot the data from Franx (1988) on NGC 1395 in the same format as Figures 2–5. NGC 1395 shows the strongest linear increase of streaming velocity of any of the galaxies examined in Franx et al. (1989) sample. Indeed, here the signature is stronger than in any of the remnants, and although this galaxy shows a misalignment of only $5^\circ \pm 3^\circ$, this strong linear increase of streaming velocity with radius suggests that it may be a merger remnant.

3.3. Misalignment Angles

The remnants, especially those from the less symmetric runs show striking misalignments between their rotation and minor axes. The minor axis for a given shell of material was taken to point in the direction of the eigenvector of the inertia tensor (of the matter in the given shell) that had the

largest eigenvalue. For an axisymmetric oblate rotator, one would expect the axis of rotation to always point along this eigenvector. In more general, triaxial distributions supported by velocity anisotropy, there need not be a correlation between the apparent rotation axis and the minor axis of the distribution.

For each of the remnants, the particles are divided into 25-radial bins such that each bin contains the same number of particles. For each bin, both the inertia tensor and the angular velocity are calculated. Finally, the angle between the angular velocity and the minor axis is determined. Thus, we calculate the misalignment angle as a function of radius for each of the remnants. Furthermore, we perform a bootstrap analysis to assess the statistical significance of the misalignments (Heyl et al. 1994).

Figure 7 provides a qualitative look at the misalignments possible in merger remnants. As expected, the angles are largest in the collisions in which the disks were not aligned with the initial orbital plane. This is another effect of the transfer of orbital angular momentum from the center to the outskirts of the remnant during a merger. For example, in remnant NB01, at small radii the angular momentum is aligned approximately with the angular momentum of one of the parent disks. As one looks at larger radii, one sees more of the relic orbital angular momentum of the system, so the angular velocity slowly drifts toward the z -axis. Figure 8 illustrates this trend. The halo particles absorb much of the angular momentum of the collision, attenuating this effect.

Kinematic misalignments are widely observed in elliptical galaxies (Franx 1988; Franx et al. 1989). Translating from

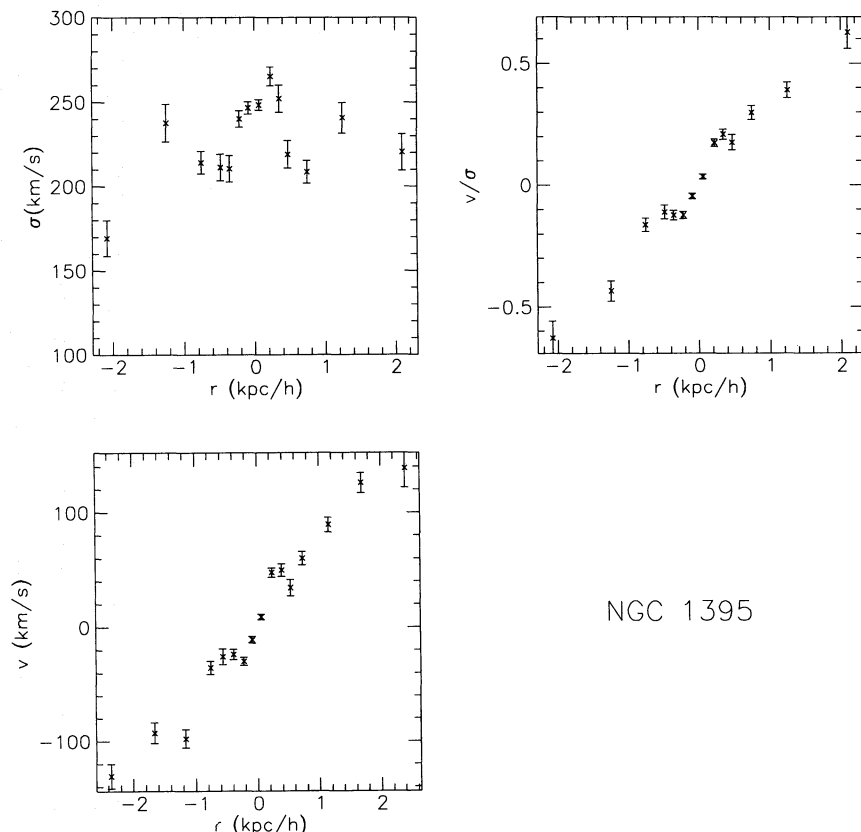


FIG. 6.—Major-axis velocity profile of the elliptical galaxy NGC 1395. Data points were taken from Franx 1988. To calculate the values of v/σ we fit the mean streaming velocities and their errors with a cubic spline and interpolated to the radii given by Franx 1988 for the measurements of σ . The effective radius (r_e) of this galaxy is $45''$ or $3.4 \text{ kpc } h^{-1}$, where h is the Hubble constant in units of $100 \text{ km s}^{-1} \text{ Mpc}^{-1}$. For comparison, r_e in the remnants is approximately 3 kpc.

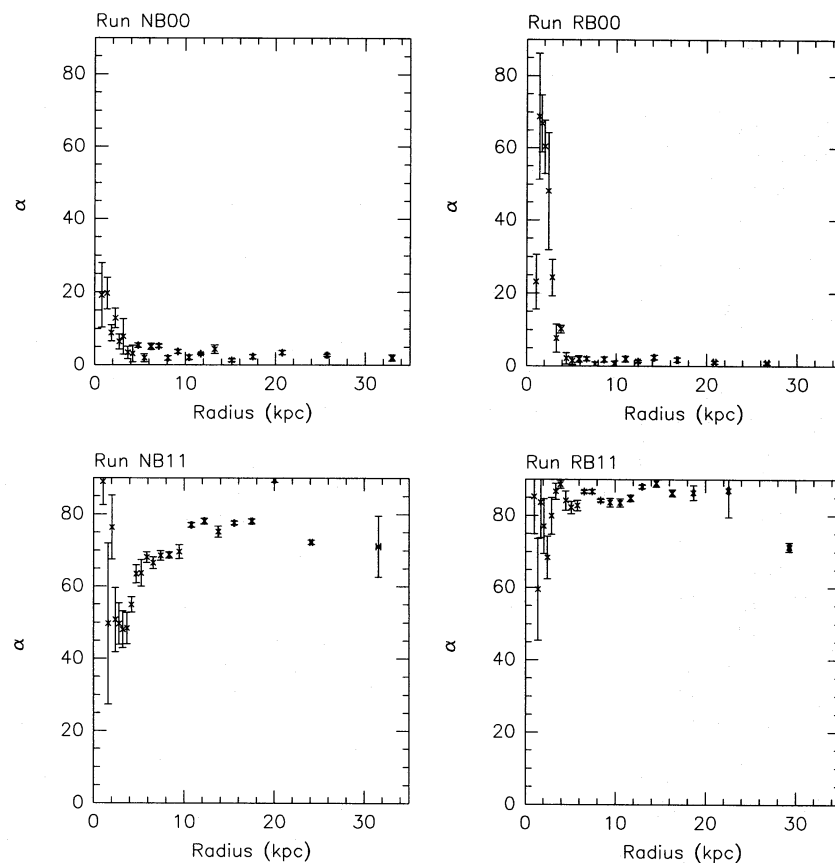


FIG. 7.—Misalignment angles (α) for the remnants NB00, RB00, NB11, and RB11. We calculate the misalignment angle by measuring the angle between the minor axis of the luminous material in the remnant within a radial bin and the angular velocity of that same material. Furthermore, we access the errors in these angles through bootstrapping. One-sigma errors are depicted.

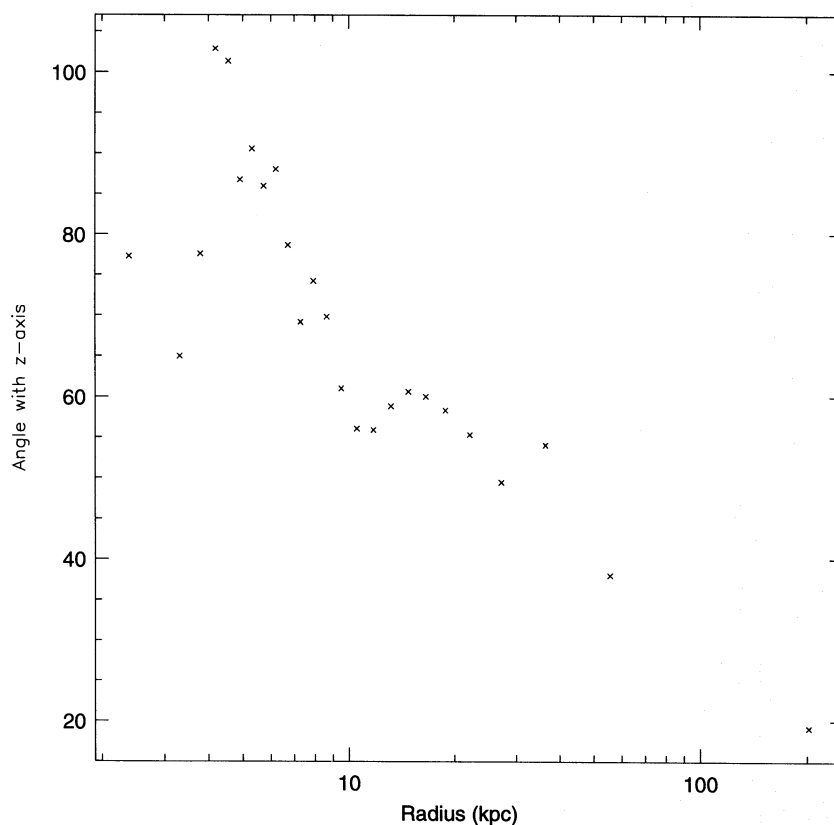


FIG. 8.—Misalignment as a function of radius for the remnant NB01. Here we show the angle between the angular momentum in successively larger shells of remnant and the z-axis (the axis of the initial orbit).

the kinematic misalignment in three dimensions to the apparent misalignment is hardly straightforward. However, qualitatively the merger remnants span the range of misalignments observed. However, the simulations fill the range of span of misalignments evenly from 0° to 90° . In the data, the misalignments are generally small (less than 20°) with only a few galaxies with 70° – 90° misalignments.

Our results agree with the findings of Barnes (1992) who also found that skew collisions resulted in larger misalignments while nearly prograde collisions left small misalignments. He also noticed that misalignment is a function of radius albeit with coarser resolution. Here we explore several new initial configurations which result in larger misalignments than Barnes found. For his innermost bin (in binding energy rather than radius), the misalignment angles range from less than 10° up to 60° . The present simulations have misalignments up to 75° or 80° . However, the general themes are similar. Mergers result in kinematic misalignments which are a function of radius and initial conditions, and are generally larger than those observed.

3.4. Orbit Structure

Orbit structure is a fundamental aspect of the kinematics of a stellar system. It is at the basis of the trends that we examined in the preceding sections. We focus on the remnants NB00, RB00, NB11, and RB11 which are the extremes of the initial conditions in our models. As we described in § 2.2, we classify the orbits into major-axis, minor-axis and box orbits depending on which axis they circulate around, if any. Figure 9 shows the distribution of the 75% most bound particles among the various orbits as a function of energy.

Some trends are immediately apparent. Nearly all of the most tightly bound particles travel along plunging box orbits, while most of the loosely bound particles travel along minor-axis tubes. Only box orbits exist in the core of a triaxial potential; consequently, we expect the most bound particles to be traveling along these orbits. For the galaxy to appear elliptical, the less bound particles must travel along the most elliptical tube orbits. The remnants whose progenitors had bulges have many more tightly bound particles and many more particles on minor-axis tube orbits. Initially, the particles in the rotating bulges are all on tightly bound minor-axis tube orbits. The merging process scatters particles to orbits nearby in energy (Spergel & Hernquist 1992), so the bulge particles end up again on tightly bound box and minor-axis tube orbits.

The initial orientation of the disks also strongly affects the orbit structure of the remnant. The remnants of skew encounters have many more particles on major-axis tube orbits; this leads us to observe larger misalignments, strong dependence of the velocity profile on orientation, and larger skewnesses in these remnants. During the skew collisions, many particles in the disks of the galaxies occupy positions in phase space that will later become part of major-axis tube orbits. By turning the galaxies relative to the orientation of the equilibrium potential, the collision can pour phase fluid into these highly inclined orbits. The collisions without this twist transfer most of the phase fluid into box and minor-axis tube orbits.

Looking at Barnes's (1992) results one sees many similarities. The remnant with the largest fraction of major-axis tubes is his remnant 2 which results from a skew merger with initial conditions similar to our RB11 which has more

major-axis tubes than the prograde collision RB00. The current simulations with rotating bulges result in remnants with more particles on minor-axis tube orbits and fewer on box or major-axis tubes than Barnes's remnants of collision of galaxies with nonrotating bulges. The two sets of simulations are complementary; there is little overlap in the initial geometries on the remnant and Barnes begins with bulge/disk/halo galaxies with nonrotating bulges. Here we collide bulgeless galaxies or galaxies with rotating bulges. Furthermore, the bulges in the current simulations are denser than those in Barnes (1992). The particles initially on minor-axis tube orbits are more tightly bound and more likely to remain on these orbits, further increasing the number of particles on minor-axis tube orbits.

By combining the two sets of simulations, it may be possible to develop a recipe to achieve a nearly arbitrary distribution of particles amongst the orbit families. However, it seems unlikely that mergers of whatever orientation can result in a remnant made mainly of particles on major-axis tube orbits, although the skew collisions can result in the plurality of particles on major-axis tube orbits as in Barnes's (1992) remnant 8. We come to the conclusion that mergers do not result in objects with "pathological" orbit structure, and possibly that triaxial figures of equilibrium must have a mixture of orbit families to be self-consistent.

4. DISCUSSION

4.1. Comparison with Previous Results

The analysis here parallels and extends that of Barnes (1992) with larger simulations, more realistic progenitors, and a greater variety of initial conditions. We concur with Barnes's conclusion that stellar dynamical mergers of disk galaxies often result in kinematic misalignments larger than those observed in common elliptical galaxies. The merger of two disk galaxies rotating prograde to their mutual orbit and with their disks aligned with the orbit may result in small misalignment angles, but these clean initial conditions are rather unlikely.

These intrinsic misalignments reflect the underlying orbit structure of the remnants. We find with Barnes (1992) that remnants of prograde encounters populate mainly the box and minor-axis tube orbits, while skew collisions populate the three orbit families more evenly. However, the presence of a bulge complicates this effect. The tightly bound bulges become a tightly bound core of stars in the remnant. This core disrupts box orbits, decimating their number in the skew collision and reducing their fraction by a factor of nearly 3 in the prograde encounter. This effect is similar to Barnes & Hernquist's (1996) mergers "con gas," where the gas forms a dense clump near the center of the remnant, and deepens the potential well in which the stars move. The presence of a dense bulge in the progenitors also reduces the number of stars on major-axis tube orbits in the remnants, again paralleling the effects of gas on the orbit distribution.

4.2. Observational Implications

The simulations indicate a variety of kinematic signatures that may be observed in elliptical galaxies to elucidate their origin. The most gross property is in the line-of-sight velocity distributions of the merger remnants. Figure 5 indicates that more violent collisions result in remnants with asymmetric line profiles. The profile is measured over a circular aperture centered on the galaxy, reducing the role of figure rotation. Furthermore, progenitors with bulges result in

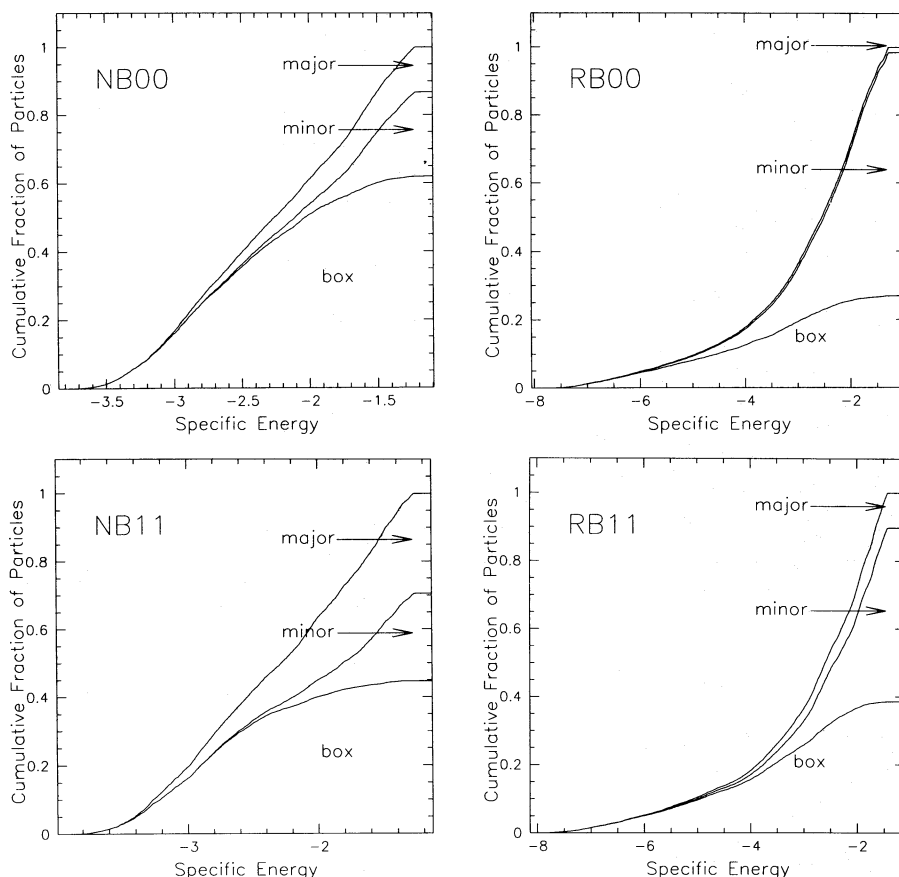


FIG. 9.—Orbit structure of the remnants NB00, RB00, NB11, and RB11. Each panel shows the cumulative fraction of particles in each type of orbit as a function of energy. Only the 75% most bound particles are depicted.

nearly symmetric line profiles. These results when combined with those of Heyl et al. (1995) indicate that the observations of integrated line profiles may be a powerful tool to understand the nature of elliptical galaxies.

When the remnants are observed in further detail, more observational tracers are uncovered. Like NGC 1395 (observed by Franx [1988]), the simulated remnants have steeply rising rotation curves with v/σ approaching one-half. Although the strength of this feature varies from remnant to remnant and viewpoint to viewpoint (and is sometimes absent), it appears to be characteristic of the hierarchical transfer of angular momentum in a major merger. Furthermore, the velocity profiles of the remnants vary strongly with the orientation, even when the remnant in the various projections appears similar. From an observational point of view, it is impossible to view a single galaxy from more than one orientation; however, galaxies which have similar projected density profiles and isophotal shapes may have vastly different projected kinematic properties. In major-merger remnants, projected kinematics and photometrics are not strongly coupled making it difficult to determine the origin of the galaxy from these data alone. With the few simulations that we have performed, we cannot determine the statistical distribution of this feature.

The observation of kinematic misalignments in elliptical galaxies probes their orbit structure. The merger remnants simulated often exhibit strong misalignments between their minor axes and their rotation axes. Franx, Illingworth, & de Zeeuw (1991) find such strong misalignments in only a small fraction of their sample. Elliptical galaxies have either few stars on major-axis orbits, or stellar populations spread

evenly in two directions. In the remnants of major mergers (except for the prograde-prograde case), a significant fraction of the particles travel along major-axis tube orbits, and furthermore, the two senses are not populated equally (Barnes 1992).

4.3. Status of the Merger Hypothesis

Major mergers reproduce many of the gross features of common elliptical galaxies. Carlberg (1986) pointed out a major shortcoming of the merger hypothesis. As a result of Liouville's theorem, mergers of stellar disks cannot produce the high phase-space densities found in cores of elliptical galaxies. However, Barnes (1988, 1992) and Hernquist (1992, 1993a) find that the presence of a bulge at the center of the progenitor galaxies avoids this phase-space constraint, prompting us to explore the detailed kinematic signatures of galaxy mergers.

In detail, we find, as Barnes (1992) found earlier, that the typical major merger would result in a galaxy with more stars orbiting on major-axis tube orbits than in observed ellipticals. This would be observed as large misalignments between the minor axis of the galaxy and its apparent rotation axis. We can look to chaotic merger histories to erase these signatures. Simulations of structure formation in the early universe (e.g., Navarro, Frenk, & White 1994) inspire a transformation of the standard merger hypothesis. According to these simulations, most present-day galaxies would have formed through the amalgamation of several galaxies over the age of the universe. Weil & Hernquist (1994) have taken a first step toward studying this process by simulating the evolution and subsequent merging of a tightly bound

group of galaxies. These multiple mergers produce remnants that closely resemble elliptical galaxies. The remnants are rounder than the typical remnants of major mergers; furthermore, they exhibit much smaller misalignments, in closer agreement with the observations of elliptical galaxies (Franx et al. 1991).

In addition, even a small amount of gas in the progenitor galaxies can drastically alter the dynamics of the stars, alleviating both the phase-space constraint and also possibly weakening kinematic misalignments in the remnants of major mergers. Unfortunately, Mihos & Hernquist (1994) have found that gas can work too well, resulting in dense knots of newly formed stars at the center of the remnants. Rather than joining smoothly onto a de Vaucouleurs profile, this starburst population produces a sharp break in the surface density profile. The prominence of these cores may be transitory or masked by dust, explaining their absence in the observations of ellipticals, or, as Mihos & Hernquist argue, mergers "con gas" may not have contributed greatly to the present-day population of elliptical galaxies. These conclusions are preliminary as yet, and it is difficult to make definitive conclusions about the connection of mergers "con gas" and the merger hypothesis.

4.4. Summary

In the immediate aftermath of a merger, the merger remnant has a number of "smoking guns" of recent violent activity: tidal tails, starbursts in its central region, and multiple shells. The focus of this paper has been to identify observational signatures that would reveal ancient violence in the formation of an elliptical long after "the corpse is cold." In an equilibrium system, the orbital distribution function of the system does not evolve. Thus, detailed observations of kinematics can reveal the formation history of a system many dynamical times after the merger event.

During the merger process, there is significant outward angular momentum transfer. This results in a merger remnant that is supported mostly by random motions in its center but can be rapidly rotating in its outer portions. In the skew encounter, v/σ exceeded 0.5 beyond 5 kpc from its center. This rapid rotation is not seen in numerical simula-

tion of galaxy formation through hierarchical collapse (Warren et al. 1992). Thus, deep long-slit spectra of ellipticals or observations of their planetary nebulae may reveal the formation history of these galaxies. This rapid rotation, however, does depend on viewing angle and merger geometry. This effect is much weaker in simulations with other merger geometries.

If an elliptical galaxy forms through the merger of two cold stellar components, as in the simulations described in this paper, the merger can populate orbital families unequally. We have quantified this effect by studying the occupation fraction of various orbital families in the merger remnant. This unequal distribution of clockwise and counterclockwise long-axis loop orbits will produce a misalignment between the spin and minor axes (Levison 1987; Barnes 1992). In our simulations, this misalignment was often quite large and often varied rapidly with radius. Warren et al. (1992) argue that most halos formed in their simulations of hierarchical collapse exhibit only small kinematic misalignments in agreement with the observations of elliptical galaxies by Franx et al. (1991).

Mergers leave several features on the kinematics of the remnants which reveal characteristics of the progenitor galaxies and their interaction. Furthermore, merger remnants exhibit many features observed in elliptical galaxies. A study of these signatures could uncover the detailed merger history of an individual elliptical galaxy, whether it formed from the recent merger of two cold stellar components or from the continuous amalgamation of smaller pieces.

This work was supported in part by the Pittsburgh Supercomputing Center, the Alfred P. Sloan Foundation, NASA theory grants NAGW-2422 and NAGW-2448, and the NSF under grants AST 90-18526, AST 91-17388, AST 88-58145 (PYI), and the Presidential Faculty Fellows Program. This work was completed as part of J. S. H.'s senior thesis and was supported by the Roundtable Senior Thesis Fund. J. S. H. would also like to acknowledge the support of the Marshall Aid Commemoration Commission. The research was performed using Starlink facilities.

REFERENCES

- Barnes, J. 1988, *ApJ*, 331, 699
 ———, 1992, *ApJ*, 393, 484
 Barnes, J., & Hernquist, L. 1996, *ApJ*, submitted
 Barnes, J., & Hut, P. 1986, *Nature*, 324, 446
 Bender, R. 1990, *A&A*, 229, 441
 Bertola, F., & Capaccioli, M. 1975, *ApJ*, 200, 439
 Binney, J., & Tremaine, S. 1987, *Galactic Dynamics* (Princeton: Princeton Univ. Press)
 Carlberg, R. G. 1986, *ApJ*, 310, 593
 Franx, M. 1988, Ph.D. thesis, Univ. Leiden
 Franx, M., & Illingworth, G. D. 1988, *ApJ*, 327, L55
 Franx, M., Illingworth, G. D., & de Zeeuw, T. 1991, *ApJ*, 383, 112
 Franx, M., Illingworth, G. D., & Heckman, T. 1989, *ApJ*, 344, 613
 Gerhard, O. E. 1993, *MNRAS*, 265, 213
 Hernquist, L. 1987, *ApJS*, 64, 715
 ———, 1990a, *J. Comput. Phys.*, 87, 137
 ———, 1990b, *ApJ*, 356, 359
 ———, 1992, *ApJ*, 400, 460
 ———, 1993a, *ApJ*, 409, 548
 ———, 1993b, *ApJS*, 86, 389
 Hernquist, L., & Spiegel, D. N. 1993, *ApJ*, 416, L9
 Hernquist, L., & Katz, N. 1989, *ApJS*, 70, 419
 Hernquist, L., & Ostriker, J. P. 1992, *ApJ*, 386, 375
 Hernquist, L., & Spiegel, D. N. 1992, *ApJ*, 397, L117
 Hernquist, L., Spiegel, D. N., & Heyl, J. S. 1993, *ApJ*, 416, 415
 Heyl, J. S., Hernquist, L., & Spiegel, D. N. 1994, *ApJ*, 427, 165
 ———, 1995, *ApJ*, 448, 64
 Hui, X., Ford, H. C., Freeman, K. C., & Dopita, M. A. 1995, *ApJ*, 449, 592
 Illingworth, G. D. 1977, *ApJ*, 218, L43
 Levison, H. F. 1987, *ApJ*, 320, L93
 Mihos, J. C., & Hernquist, L. 1994, *ApJ*, 437, L47
 Navarro, J. F., Frenk, C. S., & White, S. D. M. 1994, *MNRAS*, 267, L1
 Press, W. H., Flannery, B. P., Teukolsky, S. A., & Vetterling, W. T. 1986, *Numerical Recipes* (Cambridge: Cambridge Univ. Press)
 Rix, H.-W., & White, S. D. M. 1992, *MNRAS*, 254, 389
 Spiegel, D. N., & Hernquist, L. 1992, *ApJ*, 397, L75
 Toomre, A. 1977, in *The Evolution of Galaxies and Stellar Populations*, ed. B. M. Tinsley & R. B. Larson (New Haven: Yale Univ. Observatory), 401
 Toomre, A., & Toomre, J. 1972, *ApJ*, 178, 623
 van der Marel, R. P., & Franx, M. 1993, *ApJ*, 407, 525
 van der Marel, R. P., Rix, H.-W., Carter, D., Franx, M., White, S. D. M., & de Zeeuw, T. 1994, *MNRAS*, 268, 521
 Warren, M. S., Quinn, P. J., Salmon, J. K., & Zurek, W. H. 1992, *ApJ*, 399, 405
 Weil, M. L., & Hernquist, L. 1994, *ApJ*, 431, L79